Microscopic optical potential for exotic isotopes from chiral effective field theory

J. W. Holt, N. Kaiser, and G. A. Miller

Phys. Rev. C **93**, 064603 — Published 7 June 2016

DOI: 10.1103/PhysRevC.93.064603

Microscopic optical potential for exotic isotopes from chiral effective field theory

J. W. Holt[1,2], N. Kaiser[3] and G. A. Miller[1]
[1] *Physics Department, University of Washington, Seattle, WA*
[2] *Cyclotron Institute and Dept. of Physics and Astronomy, Texas A&M University, College Station, TX and*
[3] *Physik Department, Technische Universität München, Garching, Germany*

We compute the isospin-asymmetry dependence of microscopic optical model potentials from realistic chiral two- and three-body interactions over a range of resolution scales $\Lambda \simeq 400-500\,\mathrm{MeV}$. We show that at moderate projectile energies, $E_{\rm inv} = 110-200\,\mathrm{MeV}$, the real isovector part of the optical potential changes sign, a phenomenon referred to as isospin inversion. We also extract the strength and energy dependence of the imaginary isovector optical potential and find no evidence for an analogous phenomenon over the range of energies, $E \leq 200\,\mathrm{MeV}$, considered in the present work. Finally, we compute for the first time the leading corrections to the Lane parametrization for the isospin-asymmetry dependence of the optical potential and observe an enhanced importance at low scattering energies.

Introduction – The structure and dynamics of neutron-rich nuclei are key inputs for modeling neutron stars, core-collapse supernovae and r-process nucleosynthesis [1–8]. Elucidating the properties of highly isospin-asymmetric nuclear matter is therefore a priority in low-energy nuclear science research and a major motivation for the development of next-generation radioactive ion beam (RIB) facilities. Microscopic many-body methods [9–11] with chiral two- and three-body forces have been successful in describing the bound-state properties of neutron-rich matter. Complementary and consistent nuclear reaction models are under development [12–14], and of these, global optical potentials aim to address the broadest theory needs for interpreting RIB scattering experiments and simulating r-process nucleosynthesis. In fact, current modeling of the strong r-process favors a cold scenario in binary neutron star mergers [6–8, 15–17], where mass transfer to highly neutron-rich isotopes occurs and freeze-out is achieved more rapidly, which enhances the importance of radiative neutron capture processes in determining the final abundance pattern of r-process elements [18].

Although global phenomenological optical potentials [19–21] are well constrained close to the valley of nuclear stability, their predictive power for reactions involving exotic neutron-rich isotopes is not well understood. Elastic scattering data has been used in the past to parametrize local optical potentials in specific regions of the nuclear chart off stability, however, the most exotic and low-intensity radioactive ion beams require thick-target experiments that provide quality inelastic data only [22]. This motivates the need for accurate microscopic optical model potentials and investigations of their energy and isospin-asymmetry, $\delta_{np} = (N-Z)/A$, dependence. Identifying energy regimes in which the leading linear δ_{np} term is dominant can then be valuable for extrapolating existing phenomenological potentials away from stability.

The aim of the present work is to employ high-precision chiral two- and three-nucleon forces to study the real and imaginary volume components of the nucleon-nucleus optical model potential far from the valley of stability. The dependence on the isospin asymmetry of the target nucleus is traditionally taken to be linear and isovector in character, a parametrization known as the Lane form [23]. The isoscalar components of the optical potential are then independent of δ_{np}. We revisit these assumptions and find that subleading terms in δ_{np} (which are isoscalar and isovector for even and odd powers of δ_{np}, respectively) can be important for highly neutron-rich nuclei and particularly at the low energies most relevant for nuclear astrophysical phenomena. We study the energy dependence of these terms up to $E \simeq 200\,\mathrm{MeV}$ in anticipation of future experimental investigations of exotic isotope reactions at RIB facilities.

A phenomenon of particular interest is isospin inversion, whereby the real isovector optical potential is expected to change sign from positive at low energies to negative at higher energies. In the vicinity of isospin inversion, subleading terms proportional to δ_{np}^2 may become relevant and probe novel isospin physics. The interplay between intermediate-range attractive contributions to the nucleon-nucleon interaction and short-range repulsive contributions can give rise to a change in sign of the isoscalar optical potential at projectile energies greater than $E \sim 250\,\mathrm{MeV}$, which has been observed in calculations with microscopic nucleon-nucleon potentials [24]. The isovector contribution to the optical potential, arising from π-meson exchange and ρ-meson exchange in traditional one-boson exchange models, has a stronger relative energy dependence. In the past, semi-microscopic and microscopic optical potentials have been constructed from mean field theory [25–27] and realistic nucleon-nucleon interactions [28–33] respectively, and there is significant disagreement regarding the energy dependence of the isovector components. To date there are therefore no strong constraints on the kinematic transition region associated with isospin inversion.

In microscopic many-body theory the nucleon-nucleus optical model potential is identified with the on-shell nu-

cleon self-energy $\Sigma(\vec{r},\vec{r}\,';E)$ [34]. In the present study we compute the nucleon self-energy at second order in many-body perturbation theory employing as a starting point high-precision nuclear interactions derived from chiral effective field theory [35, 36]. Chiral nuclear potentials with momentum-space cutoffs $\Lambda \lesssim 450\,\mathrm{MeV}$ [37–39] exhibit very good perturbative behavior (comparable to renormalization-group evolved potentials [40–42]) and we also consider a potential employing a 500 MeV cutoff [36] that is used to give a conservative estimate of theoretical uncertainties associated with nonperturbative dynamics and variations in the resolution scale. Previous work has shown that chiral low-momentum potentials provide a good description of the symmetric nuclear matter saturation energy and density [39], the incompressibility and isospin-asymmetry energy [43], and the critical endpoint of the liquid-gas phase transition [44, 45]. The present approach to nuclear scattering is therefore consistent with nontrivial constraints from nuclear structure.

Isospin-asymmetry dependence of optical potentials – In the optical model for nucleon-nucleus scattering, the complicated many-body problem associated with multiple scattering through two- and three-body forces is replaced by an (elastic-scattering) equivalent complex-valued single-particle potential:

$$V(\vec{r},\vec{r}\,';E) = U(\vec{r},\vec{r}\,';E) + iW(\vec{r},\vec{r}\,';E), \qquad (1)$$

which in general is both non-local and energy-dependent. The imaginary part in Eq. (1) accounts for the presence of open inelastic scattering channels. Phenomenological optical potentials are often taken to be local and energy-dependent. The real and imaginary parts contain volume components proportional to Woods-Saxon densities $f_j(r) = 1/(1+e^{(r-R_j)/a_j})$:

$$U(r;E) = -\overline{U}(E) f_r(r), \quad W(r;E) = -\overline{W}(E) f_i(r), \quad (2)$$

where the parameters $\overline{U}_0(E), \overline{W}_0(E), R_{r,i}$ and $a_{r,i}$ vary smoothly with the mass number A of the target nucleus and the projectile energy E.

Recently chiral two- and three-nucleon forces have been used to compute the real and imaginary volume components of the optical potential for isospin-symmetric nuclear systems [12, 13]. Although the strength and energy dependence of the real component was found to be in good agreement with modern phenomenological parametrizations [21], the absorptive strength of the imaginary part from microscopic nuclear potentials was about a factor of two larger than that from phenomenology. We note that at low energies the phenomenological imaginary part is surface peaked and vanishes in the infinite matter limit. Microscopic many-body theory in the local density approximation attributes the surface imaginary part to the nonlinear density dependence of the imaginary volume component. In Fig. 1 we show the real and imaginary parts of the optical potential at nuclear matter saturation density $\rho_0 = 0.16\,\mathrm{fm}^{-3}$ from chiral nuclear potentials compared to the global fit in Ref. [21].

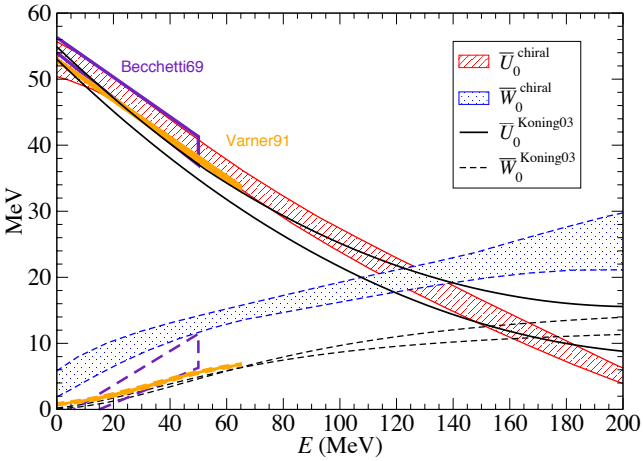

FIG. 1: (color online) Energy dependence of the real and imaginary parts of the microscopic optical model potential from chiral two- and three-body forces for symmetric nuclear matter at saturation density ρ_0. Shown for comparison are the global phenomenological potentials of Ref. [19–21].

The phenomenological "Koning" bands are obtained by varying the mass number over the range $A = 50-150$ and should not be interpreted as an uncertainty. On the other hand, the error band associated with the microscopic calculation comes from varying the resolution scale over the range $\Lambda = 414 - 500\,\mathrm{MeV}$. In Fig. 1 we have included for comparison also global optical potential parametrizations [19, 20] valid at lower energies with associated uncertainty estimates. In contrast to the results reported in Ref. [12], the single-particle energies entering in the second-order perturbative calculation are computed self-consistently via $e(q) = q^2/2M + \mathrm{Re}\,\Sigma(q, e(q))$ rather than from the effective mass plus energy shift parametrization $e(q) \simeq q^2/2M^* + \Delta$, which smears out the enhancement of the momentum-dependent effective mass at the Fermi surface [46]. From Fig. 1 we observe that the microscopic real volume component remains nearly linearly dependent on the incident energy beyond $E = 100\,\mathrm{MeV}$, in contrast to the Koning analysis in Ref. [21]. Nevertheless, the two approaches are consistent within uncertainties over a wide range of energies.

For scattering on neutron-rich nuclei, the dependence of the optical potential on the isospin asymmetry δ_{np} is crucial. The standard Lane form

$$U = U_0 + \frac{\vec{\tau}\cdot\vec{T}}{A} U_I, \qquad (3)$$

where $\vec{\tau}$ and $\vec{T}$ are the isospin operators for the projectile and target nucleus respectively, is widely used in both phenomenological and microscopic calculations. The Lane parametrization relates the elastic proton-nucleus, neutron-nucleus, and quasi-elastic charge-exchange processes. For elastic scattering the Lane form reduces to $U = U_0 - U_I \delta_{np} \tau_3$, where $\tau_3 = \pm 1$ (for protons and neutrons, respectively) is the isospin quantum number of the

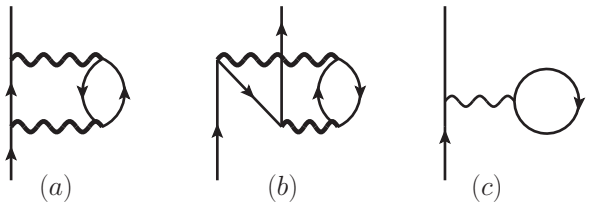

FIG. 2: Diagrams contributing to the proton and neutron self energies $\Sigma_{p,n}(q,\omega;k_f,\delta_{np})$ at first and second order in perturbation theory. The wavy line represents the antisymmetrized two-nucleon interaction $\bar{V}_{2N}$ and the thick wavy lines on the second-order diagrams represent the sum of the free-space two-body force and the density-dependent NN interaction from Refs. [47, 48].

incident nucleon.

Here we consider a more general expansion of the isospin asymmetry dependence:

$$U = U_0 - U_I\,\tau_3\delta_{np} + U_{II}\delta_{np}^2 + \mathcal{O}(\delta_{np}^3)\,. \tag{4}$$

The Hartree-Fock contribution $\Sigma_{p,n}^{(1),2N}(q;k_f,\delta_{np})$ from two-body forces, shown diagrammatically in Fig. 2(c), is obtained by generalizing the results of Ref. [12] and has the form

$$\Sigma_t^{(1),2N}(q;k_f,\delta_{np}) = \sum_1 \langle \vec{q}\vec{h}_1 s s_1 t t_1 | \bar{V}_{2N} | \vec{q}\vec{h}_1 s s_1 t t_1\rangle n_1, \tag{5}$$

where $\bar{V}_{2N}$ is the anti-symmetrized potential matrix element, $n_{p,n} = \theta(k_f(1\mp\delta_{np})^{1/3} - |\vec{h}_1|)$ is the occupation probability, and the sum is taken over the momentum $\vec{h}_1$, spin s_1, and isospin t_1 of the intermediate hole state. In the present work we compute the exact dependence of $\Sigma_{p,n}^{(1),2N}(q;k_f,\delta_{np})$ on δ_{np} and extract the linear and quadratic terms numerically.

The Hartree-Fock contributions from three-body forces are obtained by summing two particles over the filled states in the fermi sea:

$$\begin{aligned}&\Sigma_t^{(1),3N}(q;k_f,\delta_{np}) \\ &= \frac{1}{2}\sum_{12}\langle \vec{q}\vec{h}_1\vec{h}_2; s s_1 s_2; t t_1 t_2 | \bar{V}_{3N} | \vec{q}\vec{h}_1\vec{h}_2; s s_1 s_2; t t_1 t_2\rangle n_1 n_2.\end{aligned} \tag{6}$$

The next-to-next-to-leading order ($\mathrm{N^2LO}$) chiral three-body force consists of three terms, whose diagrammatic contributions to the nucleon self-energy are shown in Fig. 3. The chiral three-nucleon contact force is proportional to the low-energy constant c_E:

$$V_{3N}^{(\mathrm{ct})} = \sum_{i\neq j\neq k}\frac{c_E}{2f_\pi^4\Lambda_\chi}\vec{\tau}_i\cdot\vec{\tau}_j\,, \tag{7}$$

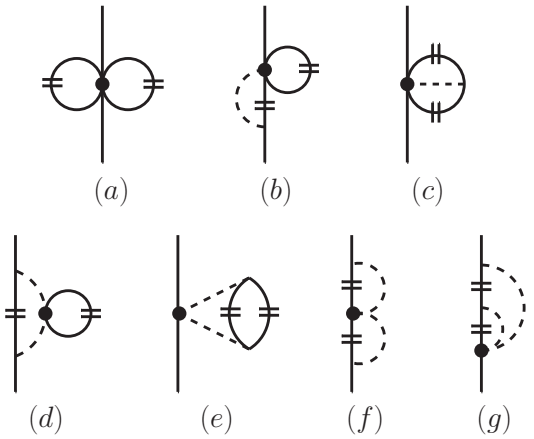

FIG. 3: Contributions to the Hartree-Fock single-particle potential from the $\mathrm{N^2LO}$ chiral three-nucleon force. The large dots represent vertices proportional to the low-energy constants c_1, c_3, c_4, c_D, c_E, and the short double-line indicates a medium insertion: $-2\pi\delta(k_0)\theta(k_f^{p,n} - |\vec{k}|)$.

where $\Lambda_\chi = 700\,\mathrm{MeV}$ and $f_\pi = 92.4$ MeV. The one-pion exchange three-body force proportional to the low-energy constant c_D has the form

$$V_{3N}^{(1\pi)} = -\sum_{i\neq j\neq k}\frac{g_A c_D}{8f_\pi^4\Lambda_\chi}\frac{\vec{\sigma}_j\cdot\vec{q}_j}{\vec{q}_j^{\,2}+m_\pi^2}\vec{\sigma}_i\cdot\vec{q}_j\,\vec{\tau}_i\cdot\vec{\tau}_j\,, \tag{8}$$

where $g_A = 1.29$ and $m_\pi = 138$ MeV. Finally, the two-pion exchange component with vertices proportional to $c_{1,3,4}$ is given by

$$V_{3N}^{(2\pi)} = \sum_{i\neq j\neq k}\frac{g_A^2}{8f_\pi^4}\frac{\vec{\sigma}_i\cdot\vec{q}_i\,\vec{\sigma}_j\cdot\vec{q}_j}{(\vec{q}_i^{\,2}+m_\pi^2)(\vec{q}_j^{\,2}+m_\pi^2)}F_{ijk}^{\alpha\beta}\tau_i^\alpha\tau_j^\beta, \tag{9}$$

where the isospin tensor is

$$F_{ijk}^{\alpha\beta} = \delta^{\alpha\beta}\left(-4c_1m_\pi^2 + 2c_3\vec{q}_i\cdot\vec{q}_j\right) + c_4\epsilon^{\alpha\beta\gamma}\tau_k^\gamma\vec{\sigma}_k\cdot(\vec{q}_i\times\vec{q}_j)\,. \tag{10}$$

The low-energy constants $c_{1,3,4}$ have been fitted (within the empirical uncertainties imposed by πN scattering) to nucleon-nucleon scattering phase shifts [36], while the c_D and c_E constants have been fitted to reproduce the binding energies of ^{3}H and ^{3}He as well as the β-decay lifetime of ^{3}H [39].

At the Hartree-Fock level, the first-order terms in δ_{np} arising from contact three-nucleon forces proportional to the low-energy constants c_E and c_D are given by

$$\begin{aligned}U_I(q,k_f) \;=\; &\frac{c_E k_f^6}{6\pi^4 f_\pi^4\Lambda_\chi} + \frac{g_A c_D m_\pi^6 u^3}{3(2\pi f_\pi)^4\Lambda_\chi}\Big\{2u - 2u^3 \\ &- \arctan 2u - \arctan(u+x) - \arctan(u-x) \\ &+\frac{1}{4u}\ln(1+4u^2) + \frac{3+5u^2-3x^2}{12x}\ln\frac{1+(u+x)^2}{1+(u-x)^2}\Big\},\end{aligned} \tag{11}$$

where $k_f^3 = 3\pi^2(\rho_n+\rho_p)/2$, $x = q/m_\pi$ and $u = k_f/m_\pi$. The 2π-exchange Hartree diagrams proportional to $c_{1,3}$

give rise to the isovector optical potential strength function

$$U_I(q,k_f) = \frac{g_A^2 m_\pi^6 u^5}{18\pi^4 f_\pi^4}\Big\{c_3 u + \frac{c_1-c_3}{2x}\ln\frac{1+(u+x)^2}{1+(u-x)^2} + \frac{(c_3-2c_1)u}{[1+(u+x)^2][1+(u-x)^2]}\Big\}, \quad (12)$$

while the 2π-exchange Fock diagrams proportional to $c_{1,3,4}$ yield

$$\begin{aligned} U_I(q,k_f) &= \frac{g_A^2 m_\pi^6 u}{9(4\pi f_\pi)^4 x^2}\Big\{-6c_1\Big[H(x,u)\,\partial_u H(x,u) \\ &+H(u,u)\,\partial_x H(u,x)\Big] + (2c_4-c_3)\Big[G(x,u)\,\partial_u G(x,u) \\ &+G(u,u)\,\partial_x G(u,x)\Big] - 2(c_3+c_4)\Big[I(x,u)\,\partial_u I(x,u) \\ &+I(u,u)\,\partial_x I(u,x)\Big] + \int_0^u d\xi\Big[18c_1\partial_u H(\xi,u)\,\partial_x H(\xi,x) \\ &+(3c_3+2c_4)\partial_u G(\xi,u)\,\partial_x G(\xi,x) + 2(3c_3-c_4) \\ &\times\partial_u I(\xi,u)\,\partial_x I(\xi,x)\Big]\Big\}, \end{aligned} \quad (13)$$

with auxiliary functions

$$\begin{aligned} G(x,u) &= \frac{4ux}{3}(2u^2-3) + 4x\big[\arctan(u+x) \\ &+\arctan(u-x)\big] + (x^2-u^2-1)\ln\frac{1+(u+x)^2}{1+(u-x)^2}, \end{aligned} \quad (14)$$

$$\begin{aligned} H(x,u) &= u(1+u^2+x^2) - \frac{1}{4x}\big[1+(u+x)^2\big] \\ &\times \big[1+(u-x)^2\big]\ln\frac{1+(u+x)^2}{1+(u-x)^2}, \end{aligned} \quad (15)$$

$$\begin{aligned} I(x,u) &= \frac{ux}{6}(8u^2+3x^2) - \frac{u}{2x}(1+u^2)^2 + \frac{1}{8}\Big[\frac{(1+u^2)^3}{x^2} \\ &-x^4+(1-3u^2)(1+u^2-x^2)\Big]\ln\frac{1+(u+x)^2}{1+(u-x)^2}, \end{aligned} \quad (16)$$

The terms second-order in δ_{np} are relatively small, and the explicit expressions are given in the Appendix.

Finally, we consider the second-order perturbative contribution from two and three-body forces, $U^{(2)}_{2N+3N}$, which is approximated by employing a density-dependent NN interaction constructed from V_{3N} as described in Refs. [47–49]. The second-order contributions, shown in Figs. 2(a) and 2(b), are given by

$$\begin{aligned} &\Sigma_t^{(2a),2N}(q,\omega;k_f,\delta_{np}) \\ &= \frac{1}{2}\sum_{123}\frac{|\langle\vec{p}_1\vec{p}_3 s_1 s_3 t_1 t_3|\bar{V}^{\rm eff}_{2N}|\vec{q}\,\vec{h}_2 s s_2 t t_2\rangle|^2}{\omega+\epsilon_2-\epsilon_1-\epsilon_3+i\eta}\bar{n}_1 n_2 \bar{n}_3 \\ &\times(2\pi)^3\delta(\vec{p}_1+\vec{p}_3-\vec{q}-\vec{h}_2), \end{aligned} \quad (17)$$

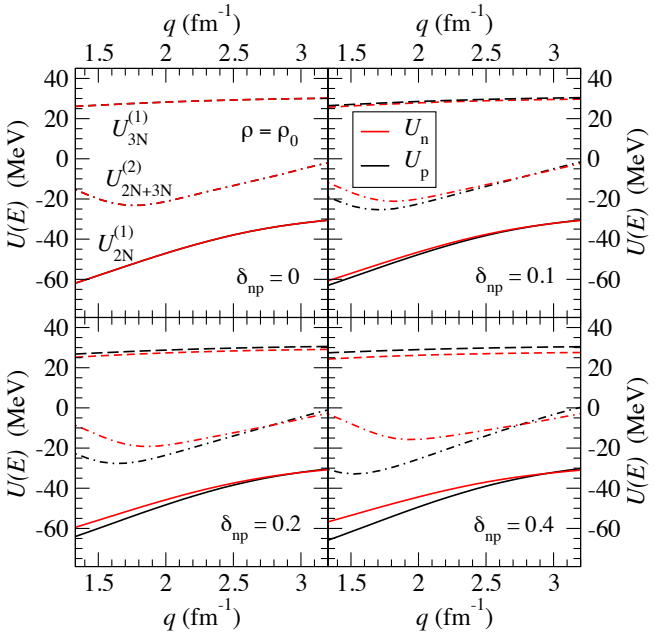

FIG. 4: (color online) Contributions to the real part of the proton and neutron optical model potentials from the n3lo450 chiral two- and three-body forces as a function of the momentum q and isospin asymmetry δ_{np} at nuclear matter saturation density ρ_0.

$$\begin{aligned} &\Sigma_t^{(2b),2N}(q,\omega;k_f,\delta_{np}) \\ &= \frac{1}{2}\sum_{123}\frac{|\langle\vec{h}_1\vec{h}_3 s_1 s_3 t_1 t_3|\bar{V}^{\rm eff}_{2N}|\vec{q}\,\vec{p}_2 s s_2 t t_2\rangle|^2}{\omega+\epsilon_2-\epsilon_1-\epsilon_3-i\eta}n_1\bar{n}_2 n_3 \\ &\times(2\pi)^3\delta(\vec{h}_1+\vec{h}_3-\vec{q}-\vec{p}_2). \end{aligned} \quad (18)$$

where $\bar{n}_k = 1-n_k$ and $\bar{V}^{\rm eff}_{2N}$ is the sum of the free-space nucleon-nucleon potential $\bar{V}_{2N}$ and the density-dependent two-body force $\bar{V}^{\rm med}_{2N}$ [47, 48]. All single-particle energies are computed self-consistently:

$$\begin{aligned} e_{p,n}(q) &= q^2/2M + \Sigma^{(1),2N}_{p,n}(q) \\ &+ \Sigma^{(1),3N}_{p,n}(q) + {\rm Re}\,\Sigma^{(2)}_{p,n}(q,e(q)). \end{aligned} \quad (19)$$

The expressions are computed for arbitrary isospin asymmetry, and the linear and quadratic terms in δ_{np} are extracted numerically.

We show in Fig. 4 the various contributions to the real part of the single-particle potential for protons and neutrons in asymmetric matter at a density of ρ_0 computed from the n3lo450 chiral NN potential. We notice that when employing the n3lo450 low-momentum chiral nuclear potential (and also the n3lo414 potential), the second-order perturbative contribution is always less than the Hartree-Fock contribution, in contrast to the behavior observed in Ref. [12] using the n3lo500 potential. We find that three-nucleon forces in general enhance

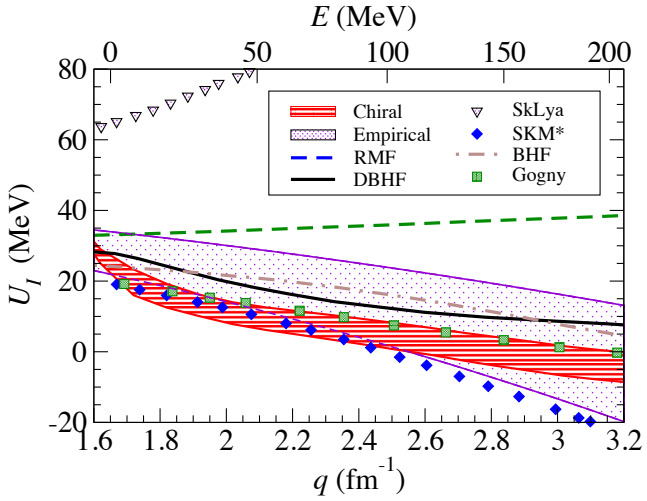

FIG. 5: (color online) Energy dependence of the isovector real optical model potential at saturation density from chiral effective field theory. Shown for comparison are the predictions of other microscopic, semi-microscopic, and phenomenological models (see Ref. [33]).

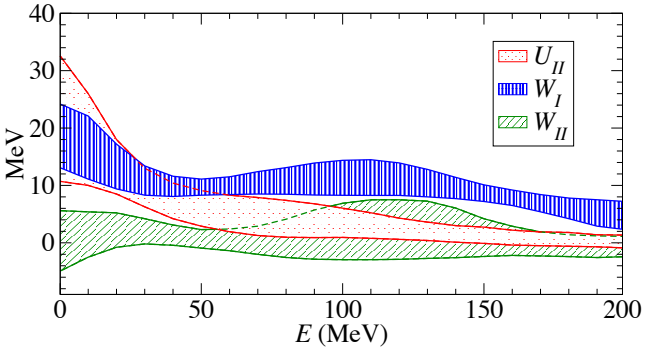

FIG. 6: Energy dependence of the isovector imaginary optical potential at saturation density from chiral two- and three-body forces. Also shown are the subleading δ^2_{np} contributions to both the real and imaginary potentials.

isospin inversion due to the repulsive character of three-body forces in homogeneous matter.

The magnitude and energy dependence of the real isovector part of the optical potential are poorly constrained by experiment. From Refs. [19–21, 25, 50–52] one finds that the magnitude is expected to decrease with energy according to $U_I = (28 \pm 6)\,\text{MeV} - (0.15 \pm 0.05)E$, which we show as the empirical band in Fig. 5. The chiral effective field theory prediction shown in Fig. 5 is consistent with the empirical constraints but has significantly smaller uncertainties, typically of about 5-10 MeV over a wide range of scattering energies. The region for isospin inversion is predicted to lie in the range $E_{\text{inv}} = 155 \pm 45\,\text{MeV}$, and the two low-momentum interactions alone would give a much narrower region of $E_{\text{inv}} = 120 \pm 10\,\text{MeV}$. The results from other microscopic many-body calculations are shown, including Brueckner-Hartree-Fock "BHF" [53] and Dirac-Brueckner-Hartree-Fock "DBHF" [33], as well as semi-microscopic mean field models: "RMF" [54], "Gogny" [55], "SKM*" [56], and "SkLya" [57]. We refer the reader to Ref. [33] for additional details and analysis.

In addition to variations in the resolution scale, also the order-by-order convergence [58, 59] in the chiral expansion provides an estimate of the theoretical uncertainty and associated cutoff artifacts. For this purpose we have computed as well the optical potential from the NLO (next-to-leading order) and N2LO chiral potentials with cutoffs $\Lambda = 450$ and 500 MeV [58]. At threshold the uncertainties for both sets of cutoffs are similar: $U_I^{450}(0) = 32 \pm 6$ MeV and $U_I^{500}(0) = 31 \pm 6$ MeV. At the isospin inversion energy the uncertainties are slightly reduced: $U_I^{450}(E_{inv}) = 0 \pm 5$ MeV and $U_I^{500}(E_{inv}) = 0 \pm 4$ MeV. Accounting for these uncertainties would not qualitatively alter the error bands shown in Fig. 5, except at low scattering energies. We also note that beyond an energy of $E \simeq 200\,\text{MeV}$, significant artifacts were observed in the calculation of the optical potential from the n3lo414 potential, suggesting a breakdown in the chiral effective field theory expansion.

In Fig. 6 we show the subleading contribution U_{II} to the real optical potential as a function of projectile energy. For low-energy scattering on neutron-rich targets we can expect an isoscalar shift of roughly $(15 - 20\,\text{MeV})\delta^2_{np}$, while for energies greater than $E > 100$ MeV the quadratic term is consistent with zero. The latter observation has the important consequence that extrapolations of phenomenological optical potentials into the neutron-rich region of the nuclear chart can be valid for energies beyond $E > 100\,\text{MeV}$. This is supported by a similar feature in the volume imaginary component, where in Fig. 6 we see that the quadratic δ^2_{np} term W_{II} is consistent with zero for all scattering energies considered. The Lane parametrization of the volume imaginary optical potential strength therefore provides an excellent approximation to the true isospin asymmetry dependence over a large range of energies. We note that since no isovector component for the volume imaginary contribution could be extracted from the most recent analyses in Refs. [20, 21] due to the uncertainties in the scattering data at large energies, our result is a prediction that may be verified at RIB facilities.

Finally, we consider the quality of fitting the isospin asymmetry dependence of the proton and neutron real optical potentials up to quadratic δ^2_{np} terms. In Fig. 7 we show as a representative example the isospin asymmetry dependence of the optical potential for a scattering energy of 50 MeV employing the n3lo450 chiral nuclear potential. For values of the isospin asymmetry up to $\delta_{np} = 0.1$ the leading contribution is isovector in character and the Lane parametrization works well. Even at $\delta_{np} = 0.2$ the second-order δ^2_{np} isoscalar contribution becomes evident. At the highest value of $\delta_{np} = 0.4$, the isoscalar δ^2_{np} term gives a contribution to the optical po-

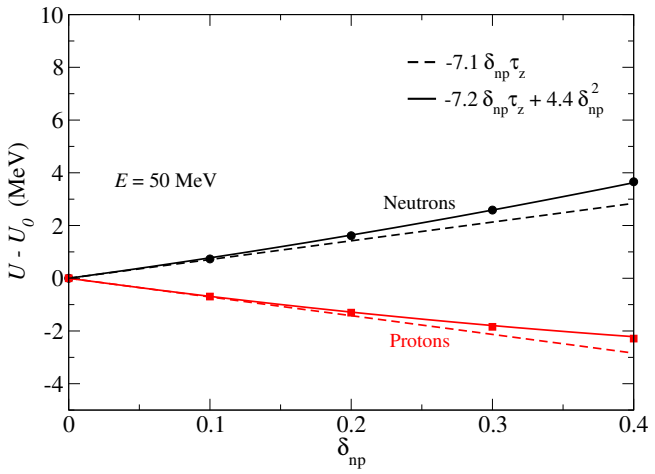

FIG. 7: Isospin asymmetry dependence of the proton and neutron real optical potentials in infinite nuclear matter at saturation density ρ_0. A scattering energy of $E = 50\,\mathrm{MeV}$ has been chosen.

tential that is about 1/4 that of the isovector contribution.

The present work lays the foundation for improved modeling of nucleon-nucleus scattering away from the valley of stability. A strong isovector component to the imaginary part of the optical potential, as found in the present study, can inhibit radiative neutron-capture cross sections on exotic nuclei [60] and strongly influence r-process nucleosynthesis in cooler environments such as the tidally ejected matter in neutron star mergers. The isovector real part of the single-particle potential (together with the isoscalar δ^2_{np} terms important at low energies) may be more relevant for neutron star inner crusts, where a lattice (or pasta structures) of neutron-rich nuclei interact with a background of free neutrons. At the higher energies attained at next-generation radioactive beam facilities, our predicted sign change in the isovector real optical potential in the energy range $110 < E_{inv} < 200\,\mathrm{MeV}$ as well as the strength of the isovector imaginary optical potential $W_I \simeq 8 - 12$ MeV can be tested.

Work supported in part by US DOE Grant No. DE-FG02-97ER-41014, the BMBF, the DFG cluster of excellence Origin and Structure of the Universe, by the DFG, NSFC (CRC110).

I. APPENDIX: δ^2_{np} CONTRIBUTIONS FROM THREE-NUCLEON FORCES

Here we present results for the quadratic δ^2_{np} corrections to the nucleon-nucleus optical potential from three-body forces at the Hartree-Fock level, which are found to be significantly smaller than the leading δ_{np} terms. The short-distance contact term contribution, shown in Fig. 3(a), has the form

$$U_{II}(q,k_f) = \frac{c_E k_f^6}{12\pi^4 f_\pi^4 \Lambda_\chi}. \tag{20}$$

The two diagrams from the one-pion exchange three-body force, Figs. 3(b) and 3(c), yield

$$\begin{aligned} U_{II}(q,k_f) &= \frac{g_A c_D m_\pi^6 u^5}{18(2\pi f_\pi)^4 \Lambda_\chi}\Big\{\frac{8u^2+3}{4u^3}\ln(1+4u^2) - 6u \\ &- \frac{3}{u} + \frac{u+x+x^{-1}}{1+(u+x)^2} + \frac{u-x-x^{-1}}{1+(u-x)^2} \\ &+ \frac{3}{2x}\ln\frac{1+(u+x)^2}{1+(u-x)^2}\Big\}. \end{aligned} \tag{21}$$

The Hartree diagrams, Figs. 3(d) and 3(e), from the two-pion exchange three-body force proportional to c_1 and c_3 give

$$\begin{aligned} U_{II}(q,k_f) &= \frac{g_A^2 m_\pi^6 u^5}{9(2\pi f_\pi)^4}\Big\{4c_3 u + \frac{6}{u}(3c_3 - 4c_1) \\ &+ \frac{8u(2c_1-c_3)}{1+4u^2} + \Big[\frac{8}{u}(c_1-c_3) + \frac{3}{2u^3}(4c_1-3c_3)\Big] \\ &\times \ln(1+4u^2) + \frac{2}{x}(c_1-c_3)\ln\frac{1+(u+x)^2}{1+(u-x)^2} \\ &+ \frac{8u(c_3-c_1)(1+x^2-u^2)}{[1+(u+x)^2][1+(u-x)^2]} \\ &+ \frac{16u^3(c_3-2c_1)(1+u^2-x^2)}{[1+(u+x)^2]^2[1+(u-x)^2]^2}\Big\}. \end{aligned} \tag{22}$$

The Fock diagrams, Figs. 3(f) and 3(g), are split into two parts depending on c_1 and $c_{3,4}$:

$$\begin{aligned} U_{II}(q,k_f) &= \frac{g_A^2 c_1 m_\pi^6 u}{3(4\pi f_\pi)^4 x^2}\Big\{H(x,u)\Big[u\,\partial_u^2 H(x,u) \\ &-2\partial_u H(x,u)\Big] + u\big[\partial_u H(x,u)\big]^2 + \partial_x H(u,x)\Big[\frac{u}{3}(3\partial_x \\ &-2\partial_u)H(x,u)\big|_{x=u} - 2H(u,u)\Big] + uH(u,u)\,\partial_u\partial_x H(u,x) \\ &+ \int_0^u d\xi\,\partial_x H(\xi,x)\Big[u\,\partial_u^2 H(\xi,u) - 2\partial_u H(\xi,u)\Big]\Big\}, \end{aligned} \tag{23}$$

$$\begin{aligned} U_{II}(q,k_f) &= \frac{g_A^2 m_\pi^6 u}{18(4\pi f_\pi)^4 x^2}\Big\{\frac{u}{3}(3c_3+2c_4)\big[\partial_u G(x,u)\big]^2 \\ &+(2c_4-c_3)G(x,u)\Big[2\partial_u G(x,u) - u\,\partial_u^2 G(x,u)\Big] + \frac{2u}{3}(3c_3 \\ &-c_4)\big[\partial_u I(x,u)\big]^2 + 2(c_3+c_4)I(x,u)\Big[u\,\partial_u^2 I(x,u) \\ &-2\partial_u I(x,u)\Big] + (c_3-2c_4)\Big[\partial_x G(u,x)\Big(\frac{u}{3}(3\partial_x G(x,u)\big|_{x=u} \\ &-2\partial_u G(x,u)\big|_{x=u} - 2G(u,u)\Big) + uG(u,u)\,\partial_u\partial_x G(u,x) \end{aligned}$$

$$+\int_0^u d\xi\,\partial_x G(\xi,x)\Big(u\,\partial_u^2 G(\xi,u)-2\partial_u G(\xi,u)\Big)\Big]+2(c_3$$
$$+c_4)\Big[\partial_x I(u,x)\Big(\frac{u}{3}(3\partial_x-2\partial_u)I(x,u)\big|_{x=u}-2I(u,u)\Big)$$
$$+uI(u,u)\,\partial_u\partial_x I(u,x)+\int_0^u d\xi\,\partial_x I(\xi,x)\Big(u\,\partial_u^2 I(\xi,u)$$
$$-2\partial_u I(\xi,u)\Big)\Big]\Big\}, \qquad (24)$$

with auxiliary functions defined in Eqs. (14)-(16).

[1] A. W. Steiner, M. Prakash, J. M. Lattimer, and P. J. Ellis, Phys. Rep. **411**, 325 (2005).
[2] R. Surman, J. Beun, G. C. McLaughlin, and W. R. Hix, Phys. Rev. C **79**, 045809 (2009).
[3] S. Brett, I. Bentley, N. Paul, R. Surman, and A. Aprahamian, Eur. Phys. J. A **48**, 184 (2012).
[4] S. Goriely, N. Chamel, H.-T. Janka, and J. M. Pearson, Astron. and Astrophys. **531**, A78 (2011).
[5] Y. Sekiguchi, K. Kiuchi, K. Kyutoku, and M. Shibata, Phys. Rev. Lett. **107**, 051102 (2011).
[6] A. Bauswein, S. Goriely, and H.-T. Janka, Astrophys. J. **773**, 78 (2013).
[7] G. Martínez-Pinedo, T. Fischer, A. Lohs, and L. Huther, Phys. Rev. Lett. **109**, 251104 (2012).
[8] L. F. Roberts, S. Reddy, and G. Shen, Phys. Rev. C **86**, 065803 (2012).
[9] S. Binder, J. Langhammer, A. Calci, P. Navratil, and R. Roth, Phys. Rev. C **87**, 021303 (2013).
[10] G. Hagen, T. Papenbrock, M. Hjorth-Jensen, and D. Dean, Rept. Prog. Phys. **77**, 096302 (2014).
[11] K. Hebeler, J. D. Holt, J. Menendez, and A. Schwenk, Ann. Rev. Nucl. Part. Sci. **65**, 457 (2015).
[12] J. W. Holt, N. Kaiser, G. A. Miller, and W. Weise, Phys. Rev. C **88**, 024614 (2013).
[13] M. Toyokawa, K. Minomo, M. Kohno, and M. Yahiro, J. Phys. G **42**, 025104 (2015).
[14] P. Navratil, S. Quaglioni, G. Hupin, C. Romero-Redondo, and A. Calci, arXiv:1601.03765 (2016).
[15] O. Korobkin, S. Rosswog, A. Arcones, and C. Winteler, Mon. Not. Roy. Astron. Soc. **426**, 1940 (2012).
[16] S. Wanajo, Y. Sekiguchi, N. Nishimura, K. Kiuchi, K. Kyutoku, and M. Shibata, Astrophys. J. **789**, L39 (2014).
[17] E. Rrapaj, J. W. Holt, A. Bartl, S. Reddy, and A. Schwenk, Phys. Rev. C **91**, 035806 (2015).
[18] M. R. Mumpower, G. C. McLaughlin, and R. Surman, Phys. Rev. C **86**, 035803 (2012).
[19] F. D. Becchetti and G. W. Greenless, Phys. Rev. **182**, 1190 (1969).
[20] R. L. Varner, W. J. Thompson, T. L. McAbee, E. J. Ludwig, and T. B. Clegg, Phys. Rept. **201**, 57 (1991).
[21] A. J. Koning and J. P. Delaroche, Nucl. Phys. **A713**, 231 (2003).
[22] L. A. Riley *et al.*, Phys. Rev. C **72**, 024311 (2005).
[23] A. M. Lane, Nucl. Phys. **35**, 676 (1962).
[24] J. P. Jeukenne, A. Lejeune, and C. Mahaux, Phys. Rept. **25**, 83 (1976).
[25] B.-A. Li, Phys. Rev. C **69**, 064602 (2004).
[26] L.-W. Chen, C. M. Ko, and B.-A. Li, Phys. Rev. C **76**, 054316 (2007).
[27] Q.-B. Shen, Y.-l. Han, and H.-R. Guo, Phys. Rev. C **80**, 024604 (2009).
[28] J. P. Jeukenne, A. Lejeune, and C. Mahaux, Phys. Rev. C **15**, 10 (1977).
[29] J.-P. Jeukenne, A. Lejeune, and C. Mahaux, Phys. Rev. C **16**, 80 (1977).
[30] I. Bombaci and U. Lombardo, Phys. Rev. C **44**, 1892 (1991).
[31] W. Zuo, I. Bombaci, and U. Lombardo, Phys. Rev. C **60**, 024605 (1999).
[32] N. Kaiser, S. Fritsch, and W. Weise, Nucl. Phys. **A700**, 343 (2002).
[33] E. N. E. vanDalen, C. Fuchs, and A. Faessler, Phys. Rev. C **72**, 065803 (2005).
[34] J. S. Bell and E. J. Squires, Phys. Rev. Lett. **3**, 96 (1959).
[35] E. Epelbaum, H.-W. Hammer, and U.-G. Meißner, Rev. Mod. Phys. **81**, 1773 (2009).
[36] R. Machleidt and D. R. Entem, Phys. Rept. **503**, 1 (2011).
[37] L. Coraggio, A. Covello, A. Gargano, N. Itaco, D. R. Entem, T. T. S. Kuo, and R. Machleidt, Phys. Rev. C **75**, 024311 (2007).
[38] L. Coraggio, J. W. Holt, N. Itaco, R. Machleidt, and F. Sammarruca, Phys. Rev. C **87**, 014322 (2013).
[39] L. Coraggio, J. W. Holt, N. Itaco, R. Machleidt, L. E. Marcucci, and F. Sammarruca, Phys. Rev. C **89**, 044321 (2014).
[40] S. K. Bogner, T. T. S. Kuo, and A. Schwenk, Phys. Rept. **386**, 1 (2003).
[41] S. K. Bogner, A. Schwenk, R. J. Furnstahl, and A. Nogga, Nucl. Phys. **A763**, 59 (2005).
[42] K. Hebeler, S. K. Bogner, R. J. Furnstahl, A. Nogga, and A. Schwenk, Phys. Rev. C **83**, 031301 (2011).
[43] J. W. Holt, N. Kaiser, and W. Weise, Nucl. Phys. **A876**, 61 (2012).
[44] C. Wellenhofer, J. W. Holt, N. Kaiser, and W. Weise, Phys. Rev. C **89**, 064009 (2014).
[45] J. W. Holt, N. Kaiser, and W. Weise, Prog. Part. Nucl. Phys. **73**, 35 (2013).
[46] G. F. Bertsch and T. T. S. Kuo, Nucl. Phys. **A112**, 204 (1968).
[47] J. W. Holt, N. Kaiser, and W. Weise, Phys. Rev. C **79**, 054331 (2009).
[48] J. W. Holt, N. Kaiser, and W. Weise, Phys. Rev. C **81**, 024002 (2010).
[49] K. Hebeler and A. Schwenk, Phys. Rev. C **82**, 014314 (2010).
[50] D. M. Patterson, R. R. Doering, and A. Galonsky, Nucl. Phys. **A263**, 261 (1976).
[51] J. Rapaport, V. Kulkarni, and R. W. Finlay, Nucl. Phys.

A330, 15 (1979).
[52] J. Rapaport, T. S. Cheema, D. E. Bainum, R. W. Finlay, and J. D. Carlson, Nucl. Phys. **A313**, 1 (1979).
[53] W. Zuo, L. G. Cao, B. A. Li, U. Lombardo, and C. W. Shen, Phys. Rev. C **72**, 014005 (2005).
[54] T. Gaitanos, M. D. Toro, S. Typel, V. Baran, C. Fuchs, V. Greco, and H. H. Wolter, Nucl. Phys. **A732**, 24 (2004).
[55] M. Kleban, B. Nerlo-Pomorska, J. F. Berger, J. Dechargé, M. Girod, and S. Hilaire, Phys. Rev. C **65**, 024309 (2002).
[56] J. Bartel, P. Quentin, M. Brack, C. Guet, and H.-B. Hakansson, Nucl. Phys. **A386**, 79 (1982).
[57] B. Cochet, K. Bennaceur, J. Meyer, P. Bonche, and T. Duguet, Int. J. Mod. Phys. E **13**, 187 (2004).
[58] F. Sammarruca, L. Coraggio, J. W. Holt, N. Itaco, R. Machleidt, and L. E. Marcucci, Phys. Rev. C **91**, 054311 (2015).
[59] E. Epelbaum, H. Krebs, and U.-G. Meissner, Eur. Phys. J. A **51**, 53 (2015).
[60] S. Goriely and J.-P. Delaroche, Phys. Lett. **B653**, 178 (2007).